



Impacts of Superalloys on the Surface Quality of Additively Manufactured Channels

Thomas M. Corbett¹

Pennsylvania State University,
 State College, PA 16801
 e-mail: tmc5980@psu.edu

Karen A. Thole

Pennsylvania State University,
 State College, PA 16801
 e-mail: kthole@psu.edu

Daniel Ryan

Solar Turbines Incorporated,
 San Diego, CA 92101
 e-mail: Ryan_Daniel@solturbines.com

Sudhakar Bollapragada

Solar Turbines Incorporated,
 San Diego, CA 92101
 e-mail: Bollapragada_Sudhakar@solturbines.com

Gas turbines feature many components that require superalloys capable of handling extreme thermal environments. Increasing the selection of materials available for these components is important to their use in these extremely high-temperature environments. This study investigated two recently developed materials intended to be used for additive manufacturing (AM), with one superalloy based on cobalt and the other on nickel. Sets of four test coupons were built using the materials, in addition to the commonly used Inconel-718, on multiple laser powder bed fusion machines. Several build conditions were varied between coupon sets, including coupon orientation, contour settings, and upskin and downskin treatment. Each set of test coupons featured four unique cooling designs to explore how different cooling technologies would be impacted by the variations in build conditions. After being built, coupons were computed tomography (CT) scanned to determine accuracy to design intent and quantify the surface roughness. The CT scans indicated that horizontally built test coupons had a significantly higher deviation from design intent and higher surface roughness than those built vertically. Results also indicated that the cobalt-based alloy consistently had a smoother surface quality with lower surface roughness compared to the nickel-based alloy. After geometric characterization, the cooling performance of the test coupons was measured experimentally. Pressure losses were found to correlate with increases in surface roughness; however, in some cases, the convective heat transfer did not increase proportionally to the pressure loss as a result of surface features significantly blocking the flow without proportionally increasing convective heat transfer. [DOI: 10.1115/1.4064468]

Keyword: heat transfer and film cooling

1 Introduction

Improving the efficiency of gas turbine engines by even a small amount can result in substantial reductions in fuel consumed to either generate thrust for aerospace applications or torque for power generation applications. One means of improving the turbine stage efficiency is by increasing the turbine inlet temperature. Developments in superalloys and sophisticated internal cooling schemes have enabled turbine inlet temperatures up to 1600 °C as of 2010, which is more than the softening temperature of the metals used to make the parts [1].

Advancements in manufacturing, such as the casting of hot section components with internal cooling features, have aided much of this development. However, not only can the casting process be expensive, but parts can take months, if not years, to manufacture [2]. Recently, some turbine manufacturers have been turning to additive manufacturing (AM), specifically laser powder bed fusion, to manufacture parts. While the low creep strength of AM components relative to single crystal cast components inhibits feasibility for AM turbine blades, other components within the hot section of the turbine under lighter loads may be able to be

manufactured via AM [3]. However, there is a limited selection of AM materials capable of handling the extreme environments in this section of the engine [4,5].

To address the limited material selection, two new superalloys have been recently developed for AM gas turbine components, with one being based on nickel and the other being based on cobalt [6]. Before using these new alloys for parts with integrated cooling features, it is important to understand how different build conditions, such as the laser parameters and part orientation, can impact the accuracy of design intent and surface roughness. To better understand this surface quality and subsequent internal heat transfer, the two new alloys were used to manufacture eight sets of four test coupons containing different internal cooling geometry. Test coupons were printed on a variety of printers with several build conditions. Internal surfaces were characterized using computed tomography scans, and test coupons were then experimentally tested to determine heat transfer and pressure loss characteristics.

2 Literature Review

The surface morphology of additive parts is highly dependent on various aspects of the build process, such as part orientation and laser process parameters. While external faces of additive parts can be smoothed through secondary machining operations, internal

¹Corresponding author.

Manuscript received September 8, 2023; final manuscript received January 3, 2024; published online March 11, 2024. Tech. Editor: David G. Bogard.

cooling geometries can be difficult to post-process due to a lack of line-of-sight access and small feature sizes. Therefore, it is important to understand how these aspects of the build process impact the as-built quality of internal additive surfaces.

Many researchers have investigated how part orientation impacted accuracy to design intent and roughness [7–10]. When parts feature surfaces that are downward facing and unsupported, known as downskin faces, it is anticipated that there will be a substantial increase in surface roughness and deviation from design intent without modifications to as-designed geometry [7]. These surface deviations are a function of the laser permeating beyond a single layer of powder due to increased powder absorptivity relative to the bulk material, resulting in dross roughness features [11]. Faces that are oriented upward and are supported beneath by solid material, known as upskin surfaces, have been shown to typically more accurately capture the design intent and have lower magnitudes of surface roughness than downskin and sidewall surfaces [8].

In addition to part orientation, there have been several studies that have investigated the influence of variations in the laser and process parameters, including changes to the laser speed, power, hatch spacing, and layer size [12–16]. These investigations identified that the surface quality was a function of the conjugate interactions between these parameters and should, therefore, be combined into a single parameter known as the volumetric energy density (VED). VED is defined as the laser power divided by the product of the laser scan speed, hatch distance, and layer size. An investigation by Wang et al. [16] showed there was a parabolic relationship between VED and surface roughness, where either too great or small VED can cause increased surface roughness. Additionally, Zhang and Yuan [17] identified that while higher VED can reduce the surface roughness of upward-facing surfaces to some extent, vertically oriented surfaces actually saw an increase in surface roughness with increasing VED.

Some researchers have also investigated curating the laser parameters for specific regions of a part. Several studies by Charles et al. [11,18] have shown that the VED used on downskin faces was directly related to the deviation from design intent and surface roughness, indicating that optimizing parameters for multiple regions of a part is important to achieve better quality surfaces. A study by Tian et al. [13] identified that the use of contour scans, which are a laser pass around the exterior surfaces of part at the end of each layer, reduced the overall surface roughness regardless of other build conditions.

Further complicating the matters of appropriate laser process parameters are variations in material. Because of differences in absorptivity, the ideal laser process parameters vary when considering different materials [19]. In addition to the surface quality, one must also consider how the material porosity, microstructure, and residual stresses are impacted by the process parameters, which have also been shown a function of the VED [19,20]. Balancing these considerations may result in parameters that provide a part with better internal grain structure and density but result in increased surface roughness.

The surface quality of additive parts has a significant impact on the cooling performance of the part. There have been many studies that have identified how the high relative surface roughness of AM microchannels augmented the cooling performance considerably [21]. One study by Kirsch et al. [22] identified that changing the material between Hastelloy X, IN718, and CoCr could cause as much as 30% variations between channel hydraulic diameters, in addition to impacting the quantity and magnitude of roughness elements present on part surfaces. These features and deviations caused the friction factor to vary by as much as 300%. Despite these substantial changes to the friction factor, heat transfer augmentations were relatively similar between designs printed from different materials, indicating that variations to the surface quality impact pressure loss more so than convective heat transfer [22].

The as-built surface quality and accuracy to design intent for designs manufactured by laser powder bed fusion (L-PBF) out of the two newly developed superalloys presented in this study have

not yet been reported. To explore the range of surface morphology that can be expected using the current state-of-the-art processing parameters for these materials, test coupons were printed in two orientations and with variations in contour settings. Computed tomography (CT) scans were completed on test coupons to identify deviations from design intent and quantify surface roughness. After characterizing the test coupons, flow testing was completed to identify how the as-built surfaces impacted the cooling performance.

3 Test Matrix Description

The primary focus of this study was to understand the as-built surface quality of two newly developed superalloys for gas turbine applications and determine the subsequent impacts this surface quality had on the cooling performance of internal cooling designs. The first superalloy used in this study was based on cobalt and was developed by University of California, Santa Barbara [23]. This alloy shows promise to exhibit higher ultimate tensile strength and durability as compared to prior Ni-based superalloys, making it a good choice for gas turbine applications [6,23,24]. The second material was based on nickel and was developed by Carpenter Technologies Corporation (Philadelphia, PA) [25], whose composition was curated to enable enhanced additive manufacturing processability. These new alloys were developed for use in the laser powder bed fusion process and had the same particle size distribution. In addition to these new alloys, IN718 was also used in this study to serve as a point of comparison for the current state-of-the-art materials available for AM gas turbine components.

To understand the as-printed quality of these new alloys, several designs were incorporated into the same general coupon shape, which is shown in Fig. 1. All coupons were designed to be 50.8 mm long, 25.4 mm wide, and 3.05 mm tall. Four different internal cooling geometry designs were investigated as part of this study, with three designs featuring wavy channels and a fourth design featuring pin fins. A diagram showing the four different designs can be seen in Fig. 2. The first wavy channel design used in this study was based on the nominal case design presented by Corbett et al. [26], with the additional two cases increasing the channel width by a factor of 1.5 and 2.0 times, respectively. Variations to the aspect ratio of the channel have been seen to alter the cooling performance of periodic channels in a prior study due to changes to the strength of the dean vortices that form along the walls of the channel [27]. Additionally, it was anticipated that the larger channel hydraulic diameter would minimize the deviation from the design intent. The nominal case channel was designed to have a hydraulic diameter of 1.27 mm, with the 1.5x width and 2.0x width channels having a diameter of 1.63 mm and 1.91 mm, respectively. Channel lengths were defined such that the flow would become fully developed throughout the length of the channel, with L/D values of approximately 30 at a minimum.

The pin fin array that was used as part of this study was based on a study by Corbett et al. [28] and featured pins that had a diamond

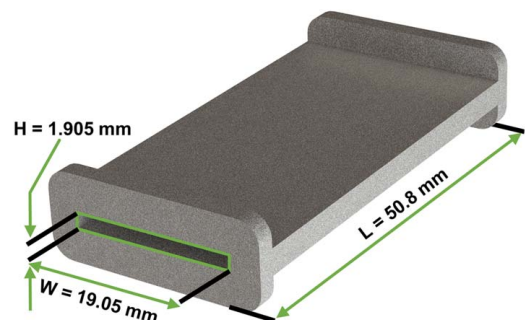


Fig. 1 General shape of all test coupons used as part of this study

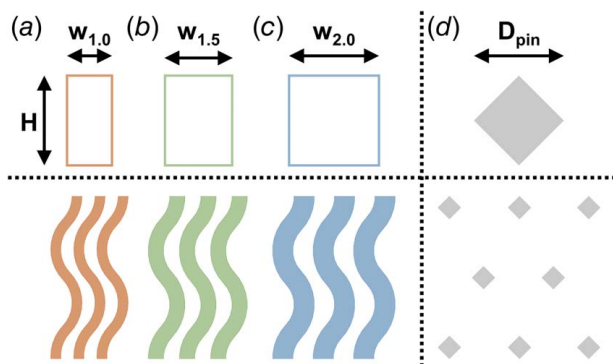


Fig. 2 Channel hydraulic diameter and internal channel geometry for the (a) nominal width, (b) 1.5 width, and (c) 2.0 width wavy channels, in addition to the (d) pin geometry and spacing for the pin fin design

cross section and were spaced at a spanwise and streamwise spacing of three pin diameters. The pin diameter was defined as the width of the maximum flow obstruction, which was designed to be 1.27 mm.

To understand the variety of surface quality that could be achieved using the two newly developed materials, a test matrix was developed that included several L-PBF machines and sets of build conditions, which are summarized in Table 1. For each variation in build conditions, all four cooling designs were printed to understand how the build conditions impacted each design independently.

The first variation to the build conditions was modifying the coupon build orientation, as can be seen in Fig. 3(a). The vertical build orientation was anticipated to enable the best quality surfaces, as much of the internal surfaces of the channel coupons would be self-supported. The horizontal build orientation was anticipated to be representative of the worst-case build direction, as much of the internal channel surface was unsupported during the build. It should be noted that for the pin fin designs, the pins were unsupported within the duct for both the vertical and horizontal print orientation.

The second variation involved enabling or disabling specialized process parameters for different regions of a given layer during the print. A breakdown of the different regions of a given layer can be seen in Fig. 3(b), wherein the core, upskin/downskin, and contour regions can be seen. Within the context of L-PBF, the core region consists of the bulk interior material of the part. Upskin and downskin regions refer to the top and bottom external surface of the part, respectively. Process parameters can be curated for the upskin and downskin regions separate from the core region, and ideally setting unique parameters should reduce roughness elements around the part and can result in improved

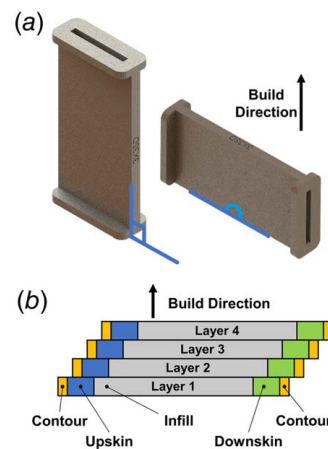


Fig. 3 (a) Vertical and horizontal print orientations and (b) schematic of different zones in a layer during a L-PBF build that may use different process parameters

accuracy to design intent. Last, a contour is a laser pass around the profile of the part for a given slice. Contours are typically used to reduce the surface roughness around the outside profile of a part.

Because there were three different materials that were used as part of this study, the process parameters used in the core region also differed and can be seen in Table 1. It should be noted that given that these new materials have only just recently been developed, the process parameters that were used as part of this study are also still under development and are expected to improve over time. Additionally, due to time and material constraints, the Ni-alloy coupons and the Co-alloy coupons were built on two different additive systems, with the Ni-alloy coupons being built on a Renishaw AM250 and the Co-alloy being built on an EOS M290. The IN718 coupons were built on a GE M2 machine by a third-party vendor, whose internal process parameters were proprietary, though are representative of the current standard parameters for current AM superalloys.

4 Geometric Characterization

All test coupons manufactured as part of this study were visually inspected immediately after manufacturing to determine if they were printed successfully. Some coupons, like those shown in Fig. 4, had almost completely blocked channels. In particular, the horizontally built coupons with specialized parameters for the “skin” regions significantly overbuilt into the channels, resulting in completely blocked flow areas. In fact, of the four sets of

Table 1 Test set build conditions

Material	Machine	Coupon orientation	Layer size (mm)	Upskin and downskin treatment	Bulk Material Settings			Contour Settings	
					Power (W)	Velocity (mm/s)	Volumetric energy density (J/mm ³)	Power (W)	Velocity (mm/s)
Ni-alloy	Renishaw	Horizontal	0.05	None	200	678	67.8	–	–
Ni-alloy	Renishaw	Horizontal	0.05	Applied	200	678	67.8	–	–
Ni-alloy	Renishaw	Horizontal	0.05	None	200	678	67.8	100	882
Ni-alloy	Renishaw	Horizontal	0.05	Applied	200	678	67.8	200	667
Ni-alloy	Renishaw	Vertical	0.05	None	200	678	67.8	100	882
Co-alloy	EOS M290	Vertical	0.03	None	167	1198	58.1	–	–
Co-alloy	EOS M290	Vertical	0.03	None	167	1198	58.1	250	400
IN718	GE M2	Vertical	–	–	–	–	–	–	–



Fig. 4 Pictures of several as-built test coupons

coupons printed horizontally, only the set with one contour and no skin treatment printed successfully. Since the blocked channels would significantly inhibit flow testing, only two sets of the coupons printed from the Ni-alloy were tested: the coupons built vertically and the coupons built horizontally with one contour and no skin treatment.

The remaining five sets of test coupons were printed without issue and underwent additional evaluation through CT scans. The CT scans were completed using a CT scanner with a voxel size of $35\ \mu\text{m}$. CT scans were post-processed using commercial software, which was able to resolve the resolution of the scan to 1/10th the voxel size or $3.5\ \mu\text{m}$ [29]. Using this software, coupon surfaces were re-constructed and exported for additional analysis using in-house post-processing code.

The wavy channel designs were processed by splitting the channel into hundreds of cross-sectional slices along the flow direction, similar to what was completed by Corbett et al. [26]. The perimeter and cross-sectional area were then determined for each slice and averaged for an entire channel, and then channels were averaged for an entire coupon. This methodology was also used to measure the wetted surface area of the channel coupons, which was used in the later analysis. The pin fin coupons were analyzed using a similar but different methodology, which sliced the coupon along the streamwise direction as well as along the length of the pins inside the duct. The slices oriented in the streamwise direction were used to calculate the duct hydraulic diameter using the same method that was described for the wavy channels. The slices oriented along the height of the channel were used to capture the pin diameter and wetted surface area for each pin independently, which was then averaged for each coupon.

To begin evaluating the as-built quality of the geometries, the deviation from design intent for the hydraulic diameter and pin size was measured, which can be seen in Fig. 5. There were significant variations in the as-built designs, with hydraulic diameters varying by as much as 15% for the nominal width channel, and pin diameter varying by over 20% for the pin fin designs. The channel with the least variation in hydraulic diameter was the 2.0x width channel, varying in diameter by less than 10% between build conditions.

To gain insight into the driving features that impacted the channel hydraulic diameter and pin diameter, the channel profile at two locations along the channel length and the midsection of two pins can be seen in Fig. 6. Starting with the channel designs, the first channel cross section was taken at plane I, shown in Figs. 6(a)–6(c). Plane I was oriented orthogonal to the build direction of the

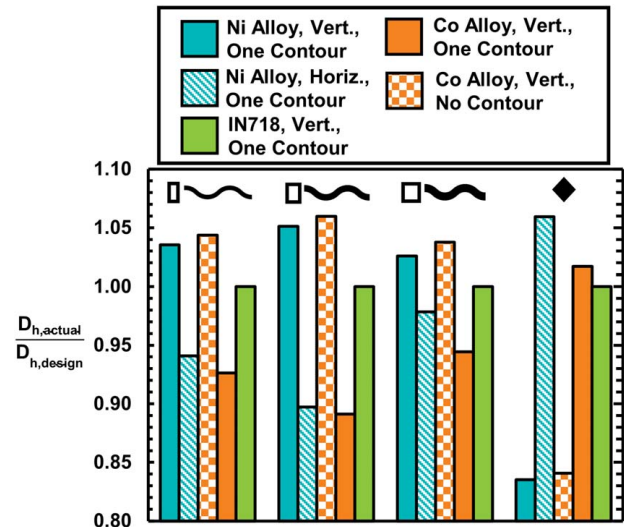


Fig. 5 Deviation from design intent for the 20 test coupons that underwent experimental testing

coupons built vertically and parallel to the build direction of the coupons built horizontally. For all three wavy channel designs printed horizontally out of the Ni-alloy, the top wall protruded significantly into the flow area, with irregular shapes forming on all walls. Since the vertically oriented Ni-alloy channel was better supported at plane I, it more closely matched the overall design intent as compared to the horizontal coupons. Despite the favorable orientation, the vertically oriented Ni-alloy channel still had significant and large irregular shapes along all walls. In contrast, the Co-alloy channels had much smoother walls, regardless of the contour setting. The difference in surface quality between the two materials was likely a function of two things: the difference in power, laser scan speed, and layer size in the contour region, as well as the difference in machine used to manufacture the two materials. Renishaw machines use a pulsed laser, whereas EOS machines use a continuous laser. Prior studies have identified parts made by a Renishaw machine have increased surface roughness relative to EOS and selective laser melting machines [30], which is suspected to be a function of the difference in laser type between machines. The two sets of Co-alloy coupons had similar build performance at the first planar location, though it should be noted that the coupons without contours had slightly larger flow areas than those built with contours. Of the build conditions evaluated, the IN718 designs printed closest to the design intent, which was anticipated due to the more refined process parameters.

The second planar location (plane II), shown in Figs. 6(e)–6(g), is at an approximately 45 deg plane to both build directions, meaning the vertically and horizontally built channels should have had a similar level of support during the build. This support is evident when comparing the Ni-alloy coupons built vertically and horizontally, as their profiles for all three wavy channel designs are very similar. The profiles are close to the design intent, indicating that the deviation from the hydraulic diameter for the horizontally built coupons that was seen in Fig. 5 was largely a function of the channel profile in the orientation shown at plane I. Conversely, the Co-alloy coupons had greater deviation from design intent than at plane I, with the coupons printed with contours being overbuilt and the coupons without contours were slightly underbuilt. This variation in print performance is also reflected in Fig. 5, where it can be seen that the samples built with one contour from the Co-alloy had a smaller than intended hydraulic diameter, and the samples without contours had a larger than intended hydraulic diameter. The magnitude of the deviation from the design intent was not a function of the width of the channel for each build condition evaluated. These deviations, therefore, had a greater impact on the hydraulic diameter

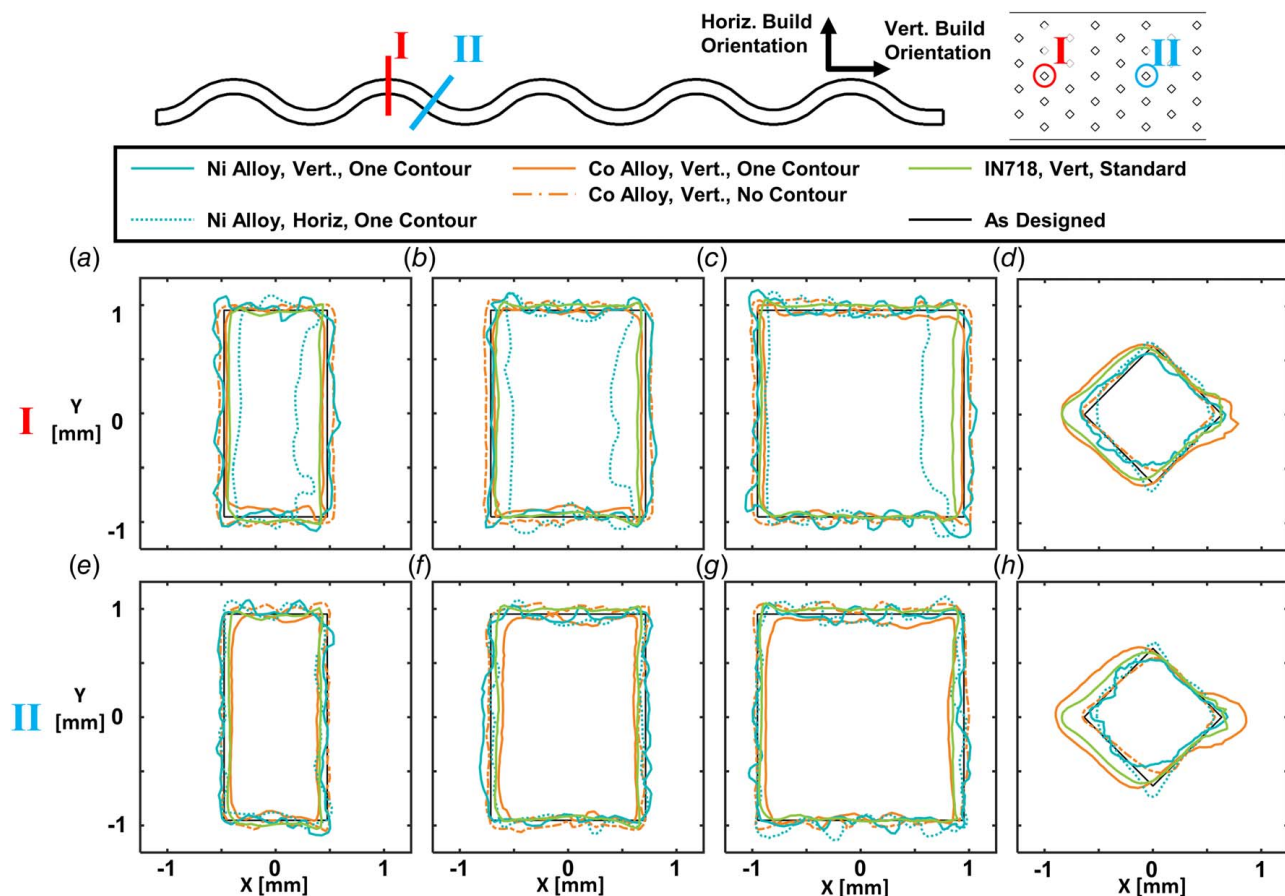


Fig. 6 (a)–(c) and (e)–(g) Wavy channel and (d) and (h) diamond pin fin profiles at two discrete locations

of the smaller width channels than the greater width channels, which is reflected in Fig. 5. Generally speaking, the profiles of the IN718 coupons show they captured the design intent more accurately than the other conditions.

The build conditions impacted the pin fins differently than they impacted the channels. The pin fins were unsupported for all test cases, resulting in significant stretching along the build direction, as shown in Figs. 6(d) and 6(h). The stretching of the pin is especially noticeable for the Co-alloy coupons printed with contours, where not only are the pin surfaces extended significantly behind the pin but also the surfaces are overbuilt in front of the pin. Despite the increase in overall pin size, the Co-alloy coupon with contours was able to more accurately capture the pin diameter than any other design, as the pin diameter was defined as the area of maximum flow obstruction. The extension into the flow area behind the pin had a significant impact on the performance, which will be discussed in later sections. Similar to the Co-Alloy, the IN718 pin fins slightly overbuilt the front of the pin, but the pins did not have the tails stretching into the flow area behind the pins. The horizontally built coupon similarly featured stretched pins, but the stretching occurred along the spanwise direction or along a given row of pins. The stretching of the pins in the horizontally built test coupon resulted in an over-sizing of the pin diameter, as well as a blunting of the front of the pin, which can be a source of significant pressure loss. Both sets of pin fin coupons made of the Co-alloy had relatively smooth pin surfaces, which is in stark contrast to those made from the Ni-alloy that featured highly irregular surfaces similar to the channels. This irregularity can cause early and localized flow detachment from the pin surface, which can significantly increase pressure loss.

To further quantify the surface quality of the coupons printed out of the new superalloys, the arithmetic mean surface roughness was

determined for the three different channel designs. While the surface roughness of the pin fin designs was also of interest, CT scans of the pin fin endwalls had substantial noise limiting the author's ability to resolve the surface. For the purposes of this study, it was anticipated that the surface roughness of the pin fin coupons was similar to that which was measured for the wavy channel designs.

The surface roughness of the coupons was measured from the same CT scan surfaces that were used to determine the channel hydraulic diameter. In-house code determined the surface roughness by first breaking up the channel into hundreds of slices, and then fitting a line to each surface in each slice and determining the average surface deviation from that line. Surface roughness values for each channel surface were then determined by averaging roughness values across all channel slices for each surface independently. Then, the channel surface roughness was found by applying a surface area-weighted average on all channel surfaces. Finally, the coupon roughness value was determined by averaging the surface roughness of all channels in a coupon.

The final roughness values found for the wavy channel coupons are presented in Fig. 7. Similar to what was seen in Fig. 6, the Ni-alloy coupons were built considerably rougher than their Co-alloy counterparts. In fact, roughness values for the Ni-alloy coupons were as much as three times as great as those built from the Co-alloy coupons. With respect to the big jump in roughness between materials, the build orientation only moderately impacted the channel surface roughness, with the horizontally built coupons being between 9% and 18% greater than those being manufactured vertically. As was seen in Fig. 6, the IN718 coupons had the lowest surface roughness of the designs, which again was anticipated based on the improved process parameters. The variation in surface roughness is most likely another result of the difference in

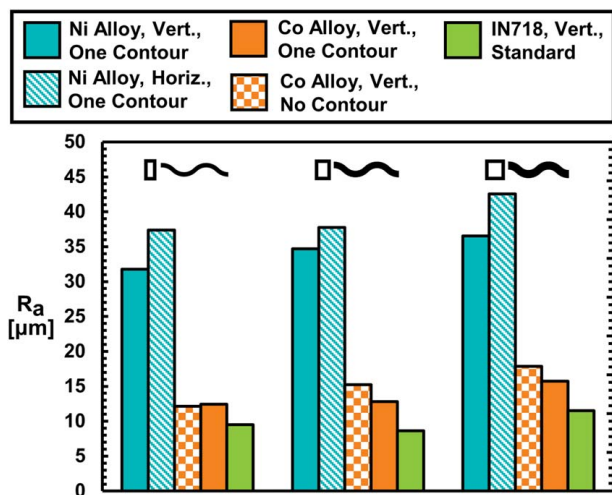


Fig. 7 Measured R_a for the wavy channel designs

additive machine and settings in the contour region during the build, as the Co-alloy coupons were built with a greater power and lower speed relative to the Ni-alloy coupons.

The final analysis to evaluate the surface quality of the different designs was to image the as-built surface using an in-house microscope, and the resulting images from this analysis are shown in Fig. 8. Starting with the 2.0x wavy channel surfaces seen in Fig. 8(a), the Ni-alloy designs have many large roughness elements that protrude significantly into the flow area, as would be expected from the results presented in Fig. 7. Both the IN718 and Co-alloy

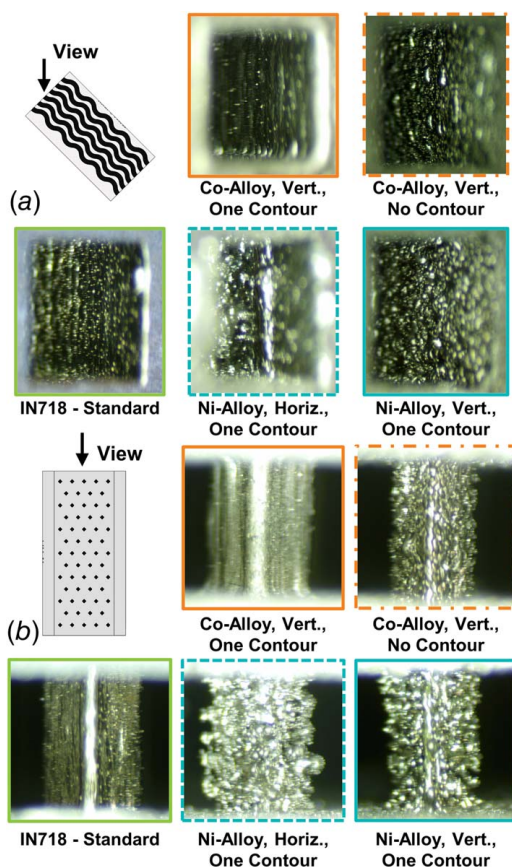


Fig. 8 Surface morphology for the (a) 2.0x width wavy channels and the (b) upskin pin fin surfaces

without contour coupons appear to have many small partially sintered particles distributed on the channel walls. The Co-alloy coupon with contours appears to have significantly fewer partially sintered particles, but layer lines are more prominent on these walls than on the other coupons. These differences in surface quality show that despite having similar magnitudes of R_a , the underlying form of the roughness is different between build conditions. The upskin surfaces of the diamond pins in the various build conditions are shown in Fig. 8(b). Mirroring the channel morphology, the Ni-alloy coupons have many large irregularly shaped nodules located along the length of the pin. The Co-alloy without contours pin fins has many small roughness features along all surfaces. In contrast, the IN718 and Co-alloy with contour coupons had relatively smooth pin surfaces with only a few partially sintered particles.

5 Thermal Conductivity

When intending to use a material for high thermal applications, it is important to quantify the material properties, especially the conductivity. To measure the thermal conductivity of the materials investigated in this study, several thermal conductivity tests were conducted according to ISO 22007-2 using a semi-infinite medium assumption. Measurements were conducted in a controlled oven at steady-state conditions, and five measurements were taken and averaged for each data point to ensure accuracy. Measurements were taken in 50 °C increments as the temperature was ramped up and down between 50 °C and 250 °C. A 95% confidence interval of these measurements indicated that the results were within 1.5% of the reported value.

The results of the thermal conductivity testing can be seen in Fig. 9. Between 50 °C and 250 °C, the thermal conductivities of the Co-alloy and Ni-alloy were between 16% and 26% lower than the conductivity of the IN718 material. However, the relative increase in thermal conductivity with an increase in temperature was similar for all three materials. The difference in thermal conductivities between the two newly developed alloys was only 3% at 50 °C and 5% at 250 °C. These results indicate that the thermal conductivity of the Co-alloy and the Ni-alloy were very similar, though it should be noted that the difference in thermal conductivity between the two materials will likely increase at higher temperatures.

6 Experimental Methods

Once the coupon surfaces were characterized, coupons were experimentally tested to capture their heat transfer and pressure

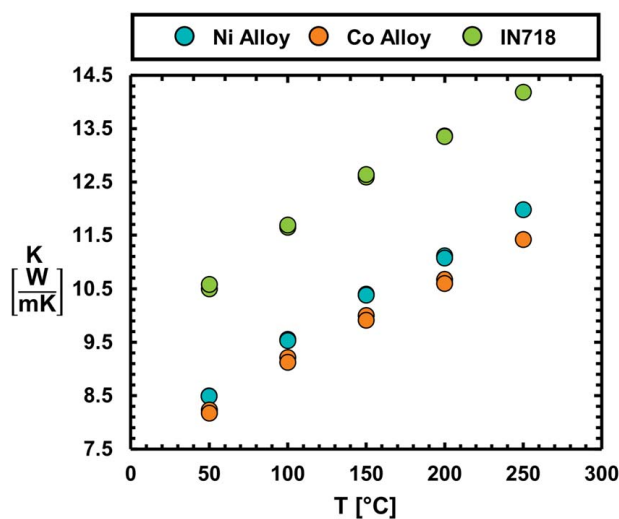


Fig. 9 Thermal conductivity of newly developed superalloys compared against standard IN718

loss performance. The test rig used in this study was the same as was reported in prior studies by the authors [26,28] and can be seen in Fig. 10.

Airflow was metered upstream of the test section using a mass flow controller, which feeds into the upstream plenum. The upstream pressure was measured using a gauge pressure sensor, and the temperature was measured through several thermal couples placed into the flow. The plenum conditioned the velocity profile of the air to be almost completely flat as it entered the test coupon. The air then passed through the test coupon and was vented to the downstream plenum, where more thermocouples placed into the flow captured the temperature, and a downstream pressure tap captured the pressure drop across the coupon. To ensure accuracy in reported values, the pressure, temperature, velocity, and density were calculated precisely at the coupon entrance and exit using isentropic flow assumptions. Back pressure in the test section was controlled using a downstream needle valve, which enabled independent control over the Mach number and Reynolds number.

For heat transfer tests, two heating assemblies were placed on either side of the test coupons to impose an isothermal wall condition. An example of one such assembly can be seen in Fig. 10. This assembly consists of a custom-designed heater placed between a foam block and a copper block. Each heater was independently powered using a variable power supply. The foam blocks were instrumented with thermocouples to capture the thermal losses of the system. The copper block featured thermocouples whose position was precisely measured. Thermal paste was used between the copper block and the coupon to minimize conduction resistance, and additional losses to the plenums were also accounted for through additional thermocouples. Using the heater power and the thermocouples located in the copper, a one-dimensional (1D) conduction analysis, as described by Stimpson et al. [21], was used to determine the temperature on the internal surface of the test coupon, accounting for the conduction losses. Using all of the measured temperatures and heat fluxes, the bulk convective coefficient was then calculated using Eq. (1).

$$h = \frac{Q_{in} - \sum Q_{loss}}{A_s \cdot \Delta T_{lm}} \quad (1)$$

Before measuring the performance of the coupons investigated in this study, the test rig was benchmarked using a traditionally manufactured smooth cylindrical channel test coupon. The friction factor measurements for the smooth coupon in the fully turbulent regime were compared against the Colebrook Equation [31], seen as Eq. (2).

$$\frac{1}{\sqrt{f}} = -2 \log_{10} \left(\frac{k_s}{3.7D_h} + \frac{2.51}{Re \sqrt{f}} \right) \quad (2)$$

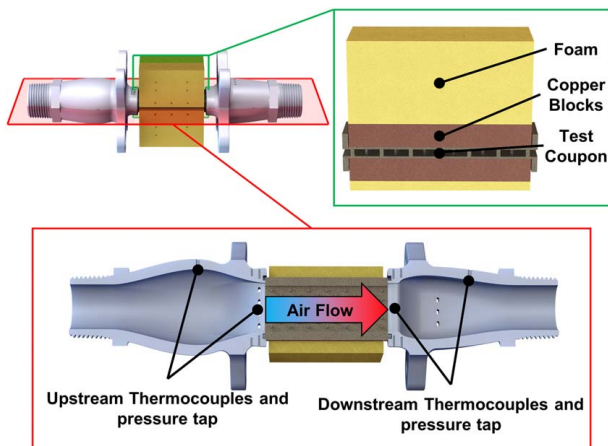


Fig. 10 Test section of test rig used in this study

It was assumed that the benchmark coupon's surface roughness, k_s , was zero. The smooth cylindrical channel friction factor, f_0 , was then found by iteratively solving Eq. (2) with no surface roughness. Heat transfer testing in the turbulent regime was similarly benchmarked by comparing the heat transfer results to the Gnielinski correlation [32], seen as Eq. (3).

$$Nu = \frac{\frac{f}{8} (Re - 1000) Pr}{1 + 12.7 \sqrt{\frac{f}{8}} (Pr^{\frac{1}{4}} - 1)} \quad (3)$$

where f_0 was used to calculate the smooth cylindrical channel Nusselt number, Nu_0 . The complete results of the benchmark testing can be seen in prior investigations by the authors [26,28], where it was seen that smooth coupon results agreed well with the stated correlations.

When determining the friction factor and the Nusselt number, either the diameter of the duct that contained the pin fin array or the wavy channel hydraulic diameter was used as the length scale. Defining the friction factor and Nusselt number using these length scales was done to enable more direct comparisons between the cooling performance augmentation in the later results sections.

7 Measurement Uncertainty

Uncertainty was calculated using the methods of propagation of error as described by Dunn [33]. Below a Reynolds number of 5000, experimental uncertainty in friction factor calculations was found to be approximately 10% but was 4% or lower for Reynolds numbers over 5000. To evaluate repeatability, coupons were completely removed test rig following testing and then reinstalled and tested again. This showed that friction factor tests were repeatable within 3%.

Experimental uncertainty was calculated to be 8% or lower for Nusselt number measurements for all Reynolds numbers, and heat transfer tests were repeated similarly to the friction factor tests and were found to also be repeatable to approximately 8%. To ensure that all of the energy entering and leaving the test rig was accounted for, the heat input from the heaters minus the measured thermal losses was compared to the heat entering the system as calculated from the first law of thermodynamics. This energy balance showed that a minimum of 95% of the energy entering and leaving the system was accounted for in all heat transfer tests, which was deemed suitable for this study.

8 Wavy Channel Cooling Performance

The friction factor augmentation and heat transfer augmentation for the wavy channel designs can be seen in Fig. 11, in addition to data from a prior study [26] featuring the same geometry. Starting with the friction factor plots shown in Figs. 11(a)–11(c), it is immediately apparent that the Ni-alloy coupons had a substantially higher friction factor augmentation than the Co-alloy coupons. In Fig. 11(a), the Ni-alloy built horizontally had an almost 5 times higher friction factor augmentation than the Co-alloy coupon with one contour, showcasing the result of the increased surface roughness of the Ni-alloy coupons. The friction factor performance mirrors the surface roughness measurements shown in the prior sections, where increases in roughness are met with increases in friction factor augmentation. It is speculated that the large roughness features that were present on the surface of the Ni-alloy parts caused frequent and substantial disturbances to the boundary layer inside of the channels, resulting in boundary layer detachment and subsequent increases in pressure loss. While the IN718 coupons had the lowest measured surface roughness, the designs performed very similarly to the Co-alloy coupons without contours. It is suspected that this similarity in performance is a function of the

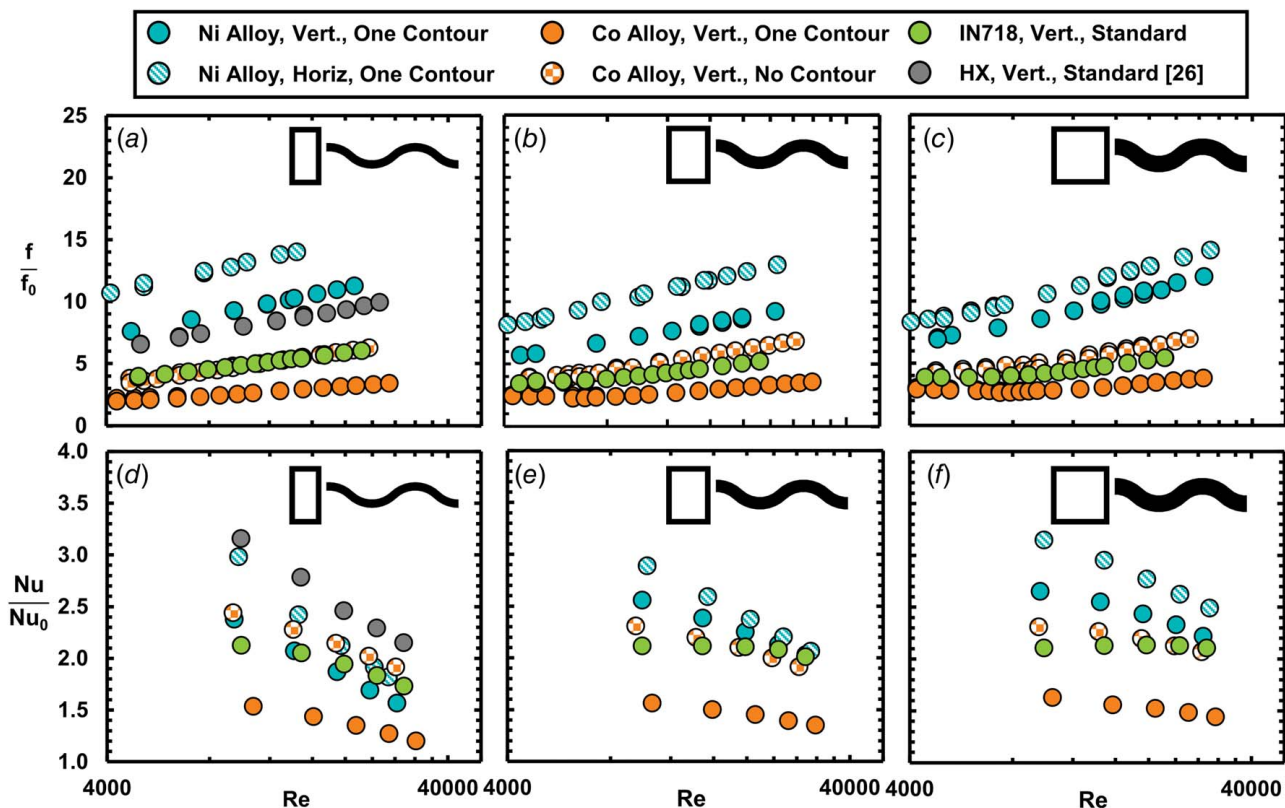


Fig. 11 (a)–(c) Friction factor augmentation and (d)–(f) Nusselt number augmentation for the three wavy channel designs

similar surface morphology that was seen in Fig. 8. Despite the differences in design, all wavy channel designs had very similar increases in friction factor with increases in Reynolds number for a given build condition. This similarity between designs indicated that the impact of the surface roughness dominated the pressure loss performance over the design of the channel.

To more clearly illustrate the difference in performance between the channel designs, the friction factor augmentation for the three wavy channel designs at two Reynolds numbers can be seen in Fig. 12. At a Reynolds number of 10,000, the friction factor augmentation was more so a function of the build conditions than the

design. In particular, the friction factor augmentation of the Co-alloy coupons without contours was almost the same regardless of the width of the wavy channel. This independence from the design was not the case with the Ni-alloy coupons, where the poor build performance paired with the high surface roughness caused significant differences in the friction factor. At a Reynolds number of 30,000, the Co-alloy coupon performance was again independent of design, with friction factor augmentation for between the three wavy channels varying by only 10%. It should be noted that at Reynolds numbers above 15,000, the channel friction factors were constant.

While the friction factor performance was consistent between the three channel designs, the heat transfer performance was not. The Nusselt number augmentation of the nominal width wavy channel is shown in Fig. 11(d). At a Reynolds number of 10,000, the horizontal Ni-alloy coupons were only moderately out-performing the Co-alloy coupons without contours, and as the Reynolds number approached 30,000, the Ni-alloy coupons performed worse than the Co-alloy coupon without contours. In contrast, the 1.5x width and 2.0x width channels, shown in Figs. 11(e) and 11(f), respectively, show the same trend in performance that was seen in the friction factor augmentation. The roughest coupons, the horizontal Ni-alloy coupons, had the highest heat transfer augmentation, and the smoothest coupons, the single contour Co-alloy coupons, had the lowest heat transfer augmentations. The IN718 coupons had very similar performance to the Co-alloy coupons without contours, as was expected based on the similar surface morphology between the test coupons. These results indicate that the high surface roughness and surface irregularity that was seen with the nominal width channels made from the Ni-alloy were ineffectively transferring heat to the mainstream flow, despite increasing the channel pressure drop. Furthermore, since these effects are not seen in the 1.5x width and 2.0x width channels, it is expected that this performance is a function of the size of the roughness elements relative to the channel hydraulic diameter.

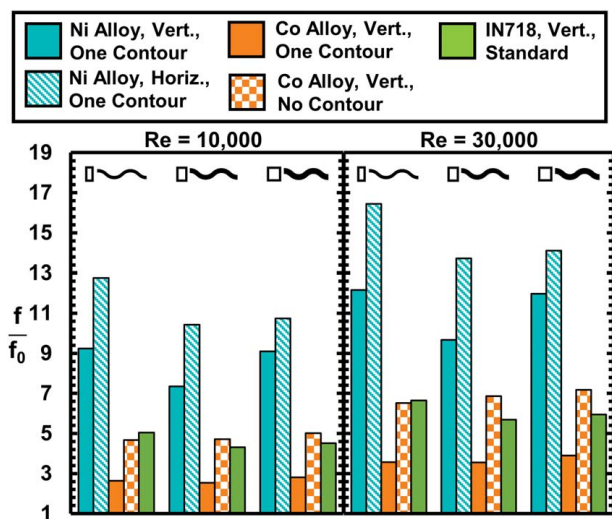


Fig. 12 Friction factor augmentation of the wavy channel coupons at Reynolds number of 10,000 and 30,000

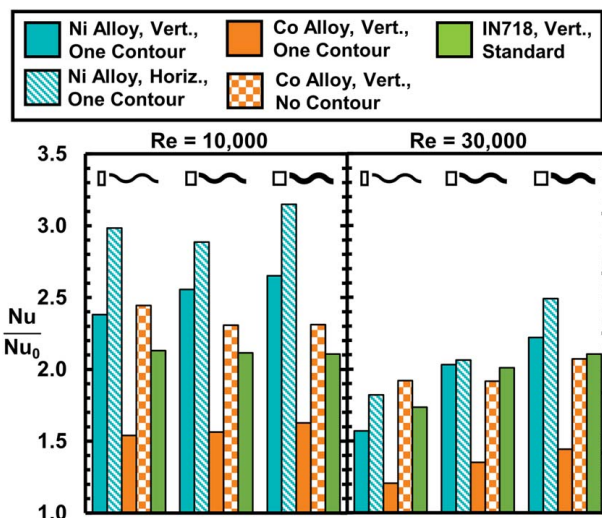


Fig. 13 Nusselt number augmentation of the wavy channel coupons at Reynolds numbers of 10,000 and 30,000

The heat transfer augmentation values at two Reynolds numbers for the three wavy channel designs can be seen in Fig. 13. Similar to the friction factor augmentations, the Nusselt number augmentations are largely a function of the material and build conditions used at a Reynolds number of 10,000, with variations in channel design only moderately impacting the heat transfer. At a Reynolds number of 30,000, the performance of the channels varies with changes in design. There is an apparent increase in Nusselt number augmentation as the channel width increases, particularly for the Ni-alloy coupons. This increase in performance indicates that wavy channels with a greater cross-sectional area may be more suitable for heat transfer applications at higher Reynolds numbers.

9 Pin Fin Array Cooling Performance

The friction factor and Nusselt number augmentations for the pin fin array design can be seen in Fig. 14, in addition to data from a prior study [28] featuring the same geometry. The friction factor augmentation for the pin fin designs was substantially greater than for the wavy channel designs. This difference in magnitude was a function of the fundamental differences in what causes pressure loss between the designs. Internal channels experience pressure loss as a function of the viscous forces that attach the flow to the walls of the channel. In addition to the pressure loss experienced at the wall, pin fin designs also introduce large flow blockages in the form of pins. These pins both locally disrupt and mix the flow, as well as develop wakes that interact with other geometry in the duct as well as other pin wakes. This critical difference in flow dynamics means that the pressure loss performance of a pin fin array is a function of both the geometry of the pin and the quality of the endwall surface. The trend and magnitude of the friction factor augmentation are, therefore, significantly different than was seen for the wavy channel coupons.

The lowest friction factor augmentation was for the Co-alloy with no contour, which can be attributed to the overall accuracy of design intent and the small size of the pin, as seen in Fig. 6. The Co-alloy pin fin coupon printed with contours can be seen to have a similar level of friction factor augmentation as the vertically printed Ni-alloy and IN718 coupons, due to the substantial deviation from the design intent of the pins. Similar to the wavy channel designs, the Ni-alloy coupon printed horizontally had the highest measured friction factor, which is suspected to be a function of the pin's elongation along the streamwise direction that was seen in Fig. 6. This elongation would not only result in an increase in the

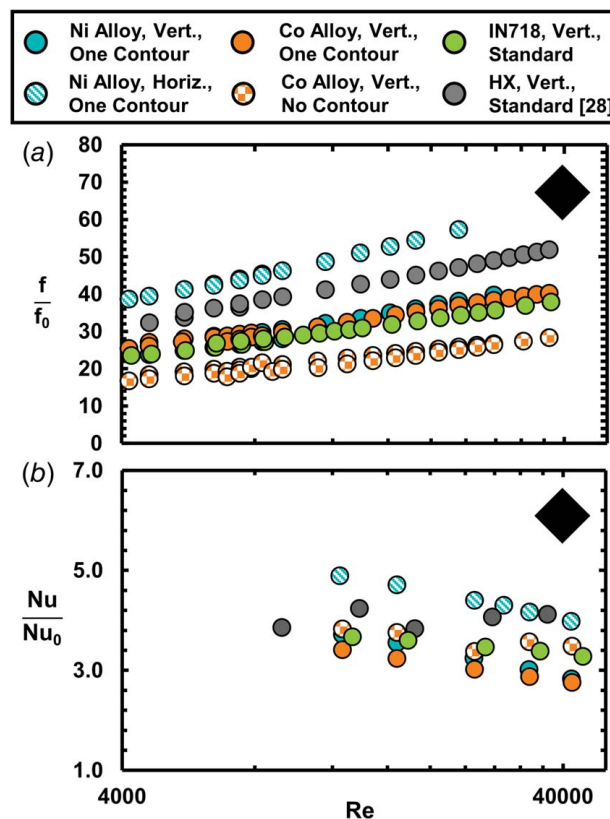


Fig. 14 (a) Friction factor augmentation and (b) Nusselt number augmentation for the pin fin designs

overall flow blockage, but also the blunter shape of the pin would induce a more significant flow detachment in the pins wake.

The heat transfer performance of the pin fin designs is shown in Fig. 14(b). Despite having a notably higher friction factor augmentation, the Co-alloy coupon built with contours and the Ni-alloy coupons built vertically both had lower Nusselt number augmentation values than the Co-alloy without contours. The increase in Nusselt number augmentation does loosely align with increases in the suspected surface roughness. It is expected, based on a prior study by the authors, that the endwall roughness played a significant role in the overall heat transfer performance of AM pin fin arrays [28]. Since it was expected that the endwall roughness of AM pin arrays drove the increased heat transfer and that the design of the pin drove the pressure loss, the heat transfer and pressure loss performance of these coupons was anticipated to be decoupled to some degree.

10 Efficiency Index of Tested Designs

Using the prior augmentations, the efficiency index as defined by Gee and Web [34] was calculated using Eq. (4).

$$\eta = \left(\frac{Nu}{Nu_0} \right) \cdot \left(\frac{f}{f_0} \right)^{-1/3} \quad (4)$$

The efficiency index is a way to indicate the relative increase in heat transfer for an increase in pressure drop. A value of one would indicate the performance of a smooth, straight, cylindrical channel. The efficiency index was plotted as a function of the Reynolds number for all tested coupons and can be seen in Fig. 15, in addition to data from prior studies featuring the same geometries [26,28]. As expected based on the Nusselt number augmentation results, the nominal width wavy channel efficiency index results, shown in Fig. 15(a), are somewhat mixed. As the Reynolds number

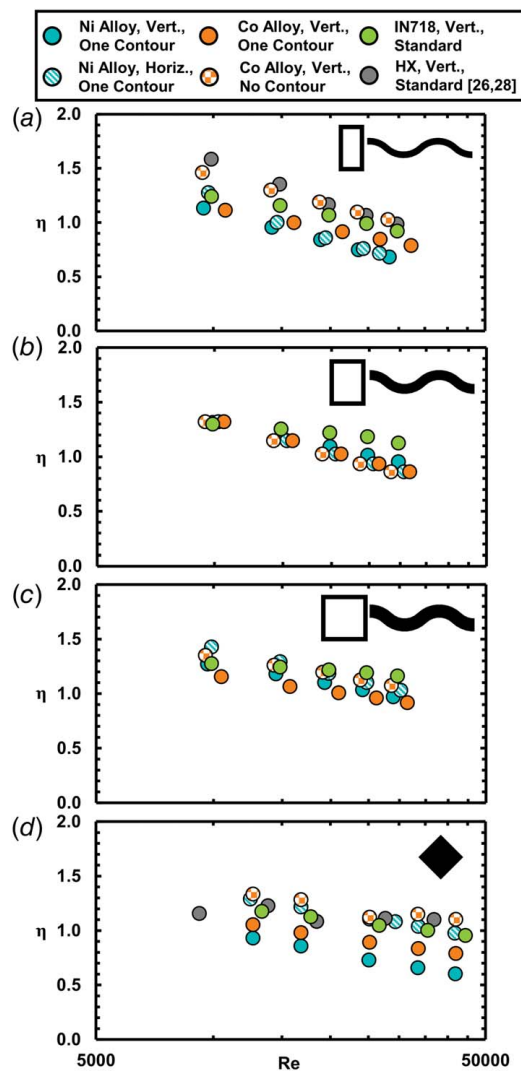


Fig. 15 Efficiency index for the (a)–(c) wavy channel and (d) pin fin array coupons as a function of Reynolds number

increased, the efficiency index of the Ni-alloy coupons decreased significantly more than the performance of the Co-alloy coupons. The efficiency index of the Ni-alloy coupons fell below one for much of the tested Reynolds range, indicating that the relative increase in pressure drop was not met with a sufficient increase in heat transfer. For the other two wavy channel designs, shown in Figs. 15(b) and 15(c), the results from all build conditions collapse onto one value. This collapse indicates that the relative increase in heat transfer for a given pressure drop was similar between these designs, and the roughness features on the surfaces of the coupons simply amplified the magnitude of the respective friction factor and Nusselt number augmentations. As the Reynolds number was increased to 30,000 for the 1.5x and 2.0x width wavy channels, the performance index was trending toward one and would likely be lower than one at even greater Reynolds numbers.

Despite the significant differences in the magnitude of the friction factor and Nusselt number augmentations between the channel and pin fin designs seen in prior figures, the efficiency index of the pin fins, shown in Fig. 15(d), is very similar to that of the wavy channels. This similar level of performance is indicative that the pin fins have a similar ratio of heat transfer to pressure loss to the wavy channel designs. There is a wider spread in the performance of the pin fin designs, however, and it is suspected that this is the result of the significant variations to the pin shape, seen in Fig. 6, and differences in the surface roughness on the endwall surfaces.

11 Conclusions

This study investigated the print surface quality of two newly developed superalloys for additive manufacturing. A variety of internal cooling designs were printed into test coupons, which were printed with a variety of build conditions. The surface quality of the designs varied substantially and was largely a function of the material, machine, laser processing parameters, and build orientation. Surface roughness was largely a function of the build conditions regardless of internal design, with the Ni-alloy coupons having significantly greater surface roughness than the Co-alloy coupons.

Thermal conductivity testing revealed that the newly developed materials had an approximately 20% lower thermal conductivity than standard IN718. Friction factor results showed that the poor surface quality of the Ni-alloy coupons caused high pressure losses for the wavy channel designs. The deviation from design intent for the pin fin designs caused the Co-alloy coupon built with contours and the Ni-alloy coupon built horizontally to have a significantly increased friction factor. Increases in friction factor were not always met with increases in heat transfer, as was the case for the wavy nominal width wavy channel built from the Ni-alloy. However, the 1.5x width and 2.0x width wavy channels did see improved heat transfer performance with increases in friction factor. Efficiency index calculations showed that the 1.5x and 2.0x width channels had a similar increase to heat transfer for a given amount of pressure loss but that the nominal width wavy channel built from the Ni-alloy had worse performance than a smooth, cylindrical channel at Reynolds numbers greater than 20,000. This reduction in performance is suspected to be a function of the large surface roughness relative to hydraulic diameter inhibiting heat transfer.

Acknowledgment

The authors of this study would like to thank Solar Turbines Incorporated, whose support made this work possible. Their insight into the project gave valuable commercial perspective. Additional thanks to Sara Mueller and Penn State's CQI for conducting all CT scans used to analyze test coupons. The research was sponsored by the US Department of Energy, Office of Energy Efficiency and Renewable Energy (EERE), Advanced Manufacturing Office, under Contract DE-AC05-00OR22725 with UT-Battelle LLC. This work was performed in part at the Oak Ridge National Laboratory's Manufacturing Demonstration Facility, an Office of Energy Efficiency and Renewable Energy user facility.

Conflict of Interest

There are no conflicts of interest.

Data Availability Statement

The datasets generated and supporting the findings of this article are obtainable from the corresponding author upon reasonable request.

Nomenclature

- f = Darcy friction factor, $f = \Delta P \frac{D_h}{L \rho u^2}$
 h = convective heat transfer coefficient, $h = \frac{Q_{in} - \sum Q_{loss}}{A_s \cdot \Delta T_{LM}}$
 k = thermal conductivity
 p = channel perimeter
 u = mass average velocity
 w = channel width
 H = channel height
 L = channel length

P = static pressure
 Q = heat transfer rate
 T = temperature
 z_{ref} = reference surface height
 z_{surf} = roughness height
 A_c = cross-sectional flow area
 A_s = surface area
 D_h = hydraulic diameter, $D_h = 4 \frac{A_c}{P}$
 D_{pin} = pin diameter
 R_a = arithmetic mean surface roughness, $R_a = \frac{1}{n} \sum_{i=1}^n |z_{\text{surf}} - z_{\text{ref}}|$
 T_{LM} = log-mean temperature, $\Delta T_{\text{LM}} = \frac{T_{\text{in}} - T_{\text{out}}}{\ln\left(\frac{T_s - T_{\text{in}}}{T_s - T_{\text{out}}}\right)}$
 Nu = Nusselt number, $\text{Nu} = h \frac{D_h}{k_{\text{air}}}$
 Pr = Prandtl number
 Re = Reynolds number, $\text{Re} = \frac{uD_h}{\nu}$

Greek Symbols

ν = kinematic viscosity
 ρ = fluid density

Subscripts

s = surface condition
 in = inlet condition
 out = outlet condition
 0 = smooth condition

References

- [1] Saravanamuttoo, H. I. H., Rogers, G., Cohen, H., and Straznicky, P., 2009, *Gas Turbine Theory*, Pearson Prentice Hall, Harlow, England; New York.
- [2] Konter, M., and Thumann, M., 2001, "Materials and Manufacturing of Advanced Industrial Gas Turbine Components," *J. Mater. Process. Technol.*, **117**(3), pp. 386–390.
- [3] Wimmer, T., Ruehmer, T., Mick, Y., Wang, L., and Weigand, B., 2019, "Experimental and Numerical Investigation on an Additively Manufactured Gas Turbine Ring Segment With an In-Wall Cooling Scheme," *ASME Turbo Expo 2019*, Phoenix, AZ, June 17–21, pp. 1–9.
- [4] Sanchez, S., Smith, P., Xu, Z., Gaspard, G., Hyde, C. J., Wits, W. W., Ashcroft, I. A., Chen, H., and Clare, A. T., 2021, "Powder Bed Fusion of Nickel-Based Superalloys: A Review," *Int. J. Mach. Tools Manuf.*, **165**, p. 103729.
- [5] Gisario, A., Kazarian, M., Martina, F., and Mehrpouya, M., 2019, "Metal Additive Manufacturing in the Commercial Aviation Industry: A Review," *J. Manuf. Syst.*, **53**, pp. 124–149.
- [6] Polonsky, A., Francis, T., Pusch, K., Echlin, M., Botman, A., Randolph, S., Geurts, R., Filevich, J., and Pollock, T., 2020, "3D Characterization of a Novel CoNi-Superalloy for Additive Manufacturing," *Microsc. Microanal.*, **26**(S2), pp. 1688–1690.
- [7] Snyder, J. C., Stimpson, C. K., Thole, K. A., and Mongillo, D. J., 2015, "Build Direction Effects on Microchannel Tolerance and Surface Roughness," *ASME J. Mech. Des.*, **137**(11), p. 111411.
- [8] Chen, Z., Wu, X., and Davies, C. H. J., 2021, "Process Variation in Laser Powder Bed Fusion of Ti-6Al-4 V," *Addit. Manuf.*, **41**, p. 101987.
- [9] Pakkanen, J., Calignano, F., Trevisan, F., Lorusso, M., Ambrosio, E. P., Manfredi, D., and Fino, P., 2016, "Study of Internal Channel Surface Roughnesses Manufactured by Selective Laser Melting in Aluminum and Titanium Alloys," *Metall. Mater. Trans. A*, **47**(8), pp. 3837–3844.
- [10] Wildgoose, A. J., Thole, K. A., Subramanian, R., Kersting, L., and Kulkarni, A., 2023, "Impacts of the Additive Manufacturing Process on the Roughness of Engine Scale Vanes and Cooling Channels," *ASME J. Turbomach.*, **145**(4), p. 041013.
- [11] Charles, A., Elkaseer, A., Thijs, L., Hagenmeyer, V., and Scholz, S., 2019, "Effect of Process Parameters on the Generated Surface Roughness of Down-Facing Surfaces in Selective Laser Melting," *Appl. Sci.*, **9**(6), p. 1256.
- [12] Calignano, F., Manfredi, D., Ambrosio, E. P., Iuliano, L., and Fino, P., 2013, "Influence of Process Parameters on Surface Roughness of Aluminum Parts Produced by DMLS," *Int. J. Adv. Manuf. Technol.*, **67**(9–12), pp. 2743–2751.
- [13] Tian, Y., Tomus, D., Rometsch, P., and Wu, X., 2017, "Influences of Processing Parameters on Surface Roughness of Hastelloy X Produced by Selective Laser Melting," *Addit. Manuf.*, **13**, pp. 103–112.
- [14] Snyder, J. C., and Thole, K. A., 2020, "Effect of Additive Manufacturing Process Parameters on Turbine Cooling," *ASME J. Turbomach.*, **142**(5), p. 051007.
- [15] Malekipour, E., and El-Mounayri, H., 2018, "Common Defects and Contributing Parameters in Powder Bed Fusion AM Process and Their Classification for Online Monitoring and Control: A Review," *Int. J. Adv. Manuf. Technol.*, **95**(1–4), pp. 527–550.
- [16] Wang, D., Liu, Y., Yang, Y., and Xiao, D., 2016, "Theoretical and Experimental Study on Surface Roughness of 316L Stainless Steel Metal Parts Obtained Through Selective Laser Melting," *Rapid Prototyp. J.*, **22**(4), pp. 706–716.
- [17] Zhang, T., and Yuan, L., 2022, "Understanding Surface Roughness on Vertical Surfaces of 316 L Stainless Steel in Laser Powder Bed Fusion Additive Manufacturing," *Powder Technol.*, **411**, p. 117957.
- [18] Charles, A., Elkaseer, A., Paggi, U., Thijs, L., Hagenmeyer, V., and Scholz, S., 2021, "Down-Facing Surfaces in Laser Powder Bed Fusion of Ti6Al4V: Effect of Dross Formation on Dimensional Accuracy and Surface Texture," *Addit. Manuf.*, **46**, p. 102148.
- [19] Zhou, Y. H., Zhang, Z. H., Wang, Y. P., Liu, G., Zhou, S. Y., Li, Y. L., Shen, J., and Yan, M., 2019, "Selective Laser Melting of Typical Metallic Materials: An Effective Process Prediction Model Developed by Energy Absorption and Consumption Analysis," *Addit. Manuf.*, **25**, pp. 204–217.
- [20] Bassoli, E., Sola, A., Celesti, M., Calcagnile, S., and Cavallini, C., 2018, "Development of Laser-Based Powder Bed Fusion Process Parameters and Scanning Strategy for New Metal Alloy Grades: A Holistic Method Formulation," *Materials*, **11**(12), p. 2356.
- [21] Stimpson, C. K., Snyder, J. C., Thole, K. A., and Mongillo, D., 2016, "Roughness Effects on Flow and Heat Transfer for Additively Manufactured Channels," *ASME J. Turbomach.*, **138**(5), p. 051008.
- [22] Kirsch, K. L., Snyder, J. C., Stimpson, C. K., Thole, K. A., and Mongillo, D., 2017, "Repeatability in Performance of Micro Cooling Geometries Manufactured With Laser Powder Bed Fusion," 53rd AIAA/SAE/ASEE Joint Propulsion Conference, Atlanta, GA, July 10–12, American Institute of Aeronautics and Astronautics, pp. 1–14.
- [23] Murray, S. P., Pusch, K. M., Polonsky, A. T., Torbet, C. J., Seward, G. G. E., Zhou, N., Forsik, S. A. J., et al., 2020, "A Defect-Resistant Co–Ni Superalloy for 3D Printing," *Nat. Commun.*, **11**(1), p. 4975.
- [24] Murray, S. P., Raeker, E. B., Pusch, K. M., Frey, C., Torbet, C. J., Zhou, N., Forsik, S. A. J., et al., 2022, "Microstructure Evolution and Tensile Properties of a Selectively Laser Melted CoNi-Base Superalloy," *Metall. Mater. Trans. A*, **53**(8), pp. 2943–2960.
- [25] Zhou, N., Dicus, A. D., Forsik, S. A. J., Wang, T., Colombo, G. A., and Epler, M. E., 2020, "Development of a New Alumina-Forming Crack-Resistant High- Γ Fraction Ni-Base Superalloy for Additive Manufacturing," *Superalloys 2020*, S. Tin, M. Hardy, J. Clews, J. Cormier, Q. Feng, J. Marcin, C. O'Brien, and A. Suzuki, eds., Springer International Publishing, Cham, pp. 1046–1054.
- [26] Corbett, T., Thole, K. A., and Bollapragada, S., 2023, "Amplitude and Wavelength Effects for Wavy Channels," *ASME J. Turbomach.*, **145**(3), p. 031011.
- [27] Comini, G., Nonino, C., and Savino, S., 2003, "Effect of Aspect Ratio on Convection Enhancement in Wavy Channels," *Numer. Heat Transfer, Part A*, **44**(1), pp. 21–37.
- [28] Corbett, T. M., Thole, K. A., and Bollapragada, S., 2023, "Impacts of Pin Fin Shape and Spacing on Heat Transfer and Pressure Losses," *ASME J. Turbomach.*, **145**(5), p. 051014.
- [29] Reinhart, C., 2011, *Industrial CT & Prevision*, Volume Graphics GmbH, Heidelberg, Germany.
- [30] Uriati, F., and Nicoletto, G., 2022, "A Comparison of Inconel 718 Obtained With Three L-PBF Production Systems in Terms of Process Parameters, As-Built Surface Quality, and Fatigue Performance," *Int. J. Fatigue*, **162**, p. 107004.
- [31] Colebrook, C. F., 1939, "Turbulent Flow in Pipes, With Particular Reference to the Transition Region Between the Smooth and Rough Pipe Laws," *J. Inst. Civ. Eng.*, **11**(4), pp. 133–156.
- [32] Gnielinski, V., 1975, "New Equations for Heat and Mass Transfer in the Turbulent Flow in Pipes and Channels," NASA STIRcon Tech. Rep. A, **41**, pp. 8–16.
- [33] Dunn, P. F., 2014, *Measurement and Data Analysis for Engineering and Science*, CRC Press, Taylor & Francis, Boca Raton.
- [34] Gee, D. L., and Webb, R. L., 1980, "Forced Convection Heat Transfer in Helically Rib-Roughened Tubes," *Int. J. Heat Mass Transfer*, **23**(8), pp. 1127–1136.